In vivo velocity vector imaging and time-resolved strain rate measurements in the wall of blood vessels using MRI

Stéphane Avril, Fabien Schneider, Chrisitan Boissier, Zhi-Yong Li

In vivo velocity vector imaging and time-resolved strain rate measurements in the wall of blood vessels using MRI

Stéphane Avril[(1)], Fabien Schneider[(2)], Christian Boissier[(3)], Zhi-Yong Li[(4)]

[(1)] Center for Health Engineering
Ecole Nationale Supérieure des Mines de Saint-Étienne
PECM - CNRS UMR 5146 ; IFRESIS - INSERM IFR 143
158 Cours Fauriel, 42023 SAINT-ÉTIENNE cedex 2, FRANCE

[(2)] Radiologie Centrale Hôpital nord
CHU de Saint Etienne
42055 SAINT-ÉTIENNE cedex 2, FRANCE

[(3)] Médecine Vasculaire Hôpital nord
CHU de Saint Etienne
42055 SAINT-ÉTIENNE cedex 2, FRANCE

[(4)] School of Biological Science and Medical Engineering, Southeast University, NANJING, 210096, CHINA

Abstract

In this paper, we present a new approach for velocity vector imaging and time-resolved measurements of strain rates in the wall of human arteries using MRI and we prove its feasibility on two examples: *in vitro* on a phantom and *in vivo* on the carotid artery of a human subject. Results point out the promising potential of this approach for investigating the mechanics of arterial tissues *in vivo*.

1 Introduction

In vivo quantification of vessel wall cyclic strain [1,2] has important applications in physiology and disease research and the design of intravascular devices.

Various ultrasound techniques have been used to detect and track the vessel wall motion. Computational techniques have mainly been based on analysis of the B-mode greyscale images [3,4], M-mode [5], analyses of the raw radio-frequency (RF) ultrasound data [6], echotracking technique [7] and Doppler techniques [8]. Recently, velocity vector imaging (VVI) has been obtained using ultrasounds [9–11]. This technique is well adapted for imaging the velocity vectors of the wall of shallow arteries, like the carotid artery [10]. VVI was achieved for deep arteries using Intravascular Ultrasound (IVUS) [11], but IVUS is a rather intrusive method [12].

Magnetic Resonance Imaging (MRI) may be a non-intrusive technique well suited to imaging of any artery. MRI was often employed to imaging of artery shape and composition [13] and its application to strain measurement in different soft tissues is not recent [14, 15]. VVI of blood flow is also commonplace using angiography

techniques like Phase Contrast MRI (PC-MRI) [16]. However, VVI of artery walls using MRI is still scarce and limited. It may be achieved:

1. either measuring velocities or deformations in the thickness of arteries by PC-MRI [17] or tagging [18] but this is only feasible for thick arteries given that the smallest reachable pixel size in clinical conditions is around 0.4 mm. For instance, this is well adapted for VVI in the heart [9, 19] or the thoracic aorta [17]. This principle is at the origin of strain encoding sequences [20];
2. or tracking the luminal boundary of the vessel over time [21, 22] but this can only be accurate using subpixel techniques for tracking the wall.

This study is aimed at addressing the issue of subpixel tracking by applying the optical flow theory onto the magnitude of MRI scans. Eventually, time-resolved VVI is obtained and the strain rate is derived throughout the whole cardiac cycle. Applications to the human common carotid artery (CCA) are shown for the sake of feasibility proof.

2 Materials and Methods

A continuous intensity (or magnitude) field $I(x,y,t)$ is obtained around a given artery using the procedure detailed in Appendix 1 (Section 8). Thanks to this intensity field, the location of the artery wall is tracked over time during the cardiac cycle and the average strain $\varepsilon(t)$ of the artery is deduced according to the procedure detailed in Appendix 2 (Section 9). This approach is named the *segmentation approach* further.

For the purpose of investigating artery mechanics, it is necessary to characterize the velocity of the wall and the strain rate $\dot{\varepsilon}(t)$ throughout the cardiac cycle. For this, an original approach has been specifically developed, without requiring any time differentiation of the artery location and of $\varepsilon(t)$. This approach, which is based on the theory of optical flow [23]), is named further the *mag-flow approach*. Indeed, the conservation of the signal magnitude according to the theory of optical flow states:

$$v_x(x,y,t)\frac{\partial I}{\partial x}(x,y,t) + v_y(x,y,t)\frac{\partial I}{\partial y}(x,y,t) + \frac{\partial I}{\partial t}(x,y,t) = 0 \tag{1}$$

where $v_x(x,y,t)$ and $v_y(x,y,t)$ are the two in-plane Eulerian components of the material velocity at point (x,y) and time t.

Using the polar coordinate system defined in Eq. 11 (Appendix 2), it may be written:

$$\begin{cases} v_x(x,y,t) = \dfrac{dr}{dt}(x,y,t)\cos(\theta) - \dfrac{\partial r}{\partial \theta}(x,y,t)\sin(\theta)\dfrac{d\theta}{dt} \\ v_y(x,y,t) = \dfrac{dr}{dt}(x,y,t)\sin(\theta) + \dfrac{\partial r}{\partial \theta}(x,y,t)\cos(\theta)\dfrac{d\theta}{dt} \end{cases} \tag{2}$$

The combination of Eq. 1 and Eq. 2 yields:

$$\frac{dr}{dt}\underbrace{\left[\cos(\theta)\frac{\partial I}{\partial x}(x,y,t) + \sin(\theta)\frac{\partial I}{\partial y}(x,y,t)\right]}_{\frac{\partial I}{\partial r}} + \frac{d\theta}{dt}\underbrace{\frac{\partial r}{\partial \theta}\left[-\sin(\theta)\frac{\partial I}{\partial x}(x,y,t) + \cos(\theta)\frac{\partial I}{\partial y}(x,y,t)\right]}_{\frac{\partial I}{\partial \theta}} = -\frac{\partial I}{\partial t}(x,y,t) \tag{3}$$

The magnitude of the MRI signal is almost constant inside and outside the artery, with larger values inside the artery than outside. Accordingly, the following inequality is valid along the curve of the artery wall: $\frac{\partial I}{\partial \theta} \ll \frac{\partial I}{\partial r}$.

Therefore, for all the points belonging to the artery wall $(x = r(\theta)\cos(\theta), y = r(\theta)\sin(\theta))$, the following simplification is valid for computing locally the radial velocity:

$$\frac{dr}{dt}(x,y,t) = \dot{r}(x,y,t) = -\frac{\frac{\partial I}{\partial t}(x,y,t)}{\cos(\theta)\frac{\partial I}{\partial x}(x,y,t) + \sin(\theta)\frac{\partial I}{\partial y}(x,y,t)} \tag{4}$$

Eventually, the average strain rate of the artery at time t, considering the reference state at time t_1, is:

$$\begin{aligned} \dot{\varepsilon}(t) &= \frac{\dot{L}(t)}{L(t_1)} \\ &= \frac{1}{L(t_1)}\int_0^{2\pi} \dot{r}\, d\theta \\ &= -\frac{1}{L(t_1)}\int_0^{2\pi} \frac{\frac{\partial I}{\partial t}(r(\theta,t)\cos(\theta), r(\theta,t)\sin(\theta), t)}{\cos(\theta)\frac{\partial I}{\partial x}(r(\theta,t)\cos(\theta), r(\theta,t)\sin(\theta), t) + \sin(\theta)\frac{\partial I}{\partial y}(r(\theta,t)\cos(\theta), r(\theta,t)\sin(\theta), t)} d\theta \end{aligned} \tag{5}$$

3 Results

As a preliminary step, magnitude images are synthesized computationally in order to test the mag-flow approach. The results prove that the radial velocities are assessed with less than 1% error with the synthesized data.

Then, the mag-flow approach is tested on real MRI scans. Examples of magnitude images are shown in Fig. 1 for an arterial phantom and for a real *in vivo* experiment. Both experiments are described in Appendix 1..

After deriving the contour of the wall by the segmentation approach, the radial velocity is computed throughout the cardiac cycle using the mag-flow approach. Results are shown in Fig. 2. For this, R_x and R_y are set to value 1.2 and R_t is set to value 2. In the phantom experiment, only the outer contour is considered in the displayed results for a better visualization.

It is interesting to notice that, in the *in vivo* experiment, the deformation is not a uniform swelling or shrinking all around the left common carotid artery (CCA). For the in vivo experiment, the part of the left CCA which is the farthest from the jugular vein has almost no velocity whereas the part close to the jugular vein moves significantly towards the left and comes back. The same effect occurs symmetrically for the right CCA. The average radius, denoted $R(t)$, can be deduced either using the segmentation or the mag-flow approach (for this latter, time integration is required), according to:

$$R(t) = \underbrace{\frac{1}{2\pi}\int_0^{2\pi} r(\theta,t)d\theta}_{\text{segmentation approach}} = \underbrace{R(t_1) + \frac{1}{2\pi}\int_0^t \left[\int_0^{2\pi} \dot{r}(\theta,t)d\theta\right] dt}_{\text{mag-flow approach}} \tag{6}$$

Results are shown for both the arterial phantom and the subject in Fig. 3. There is a good agreement between both approaches. This proves that, in average, the radial velocities computed by the mag-flow approach are in good agreement with the motions of the segmented contours. However, the curve of the mag-flow approach is much smoother.

The average strain rate is computed throughout the cardiac cycle, either using the segmentation approach, or using our novel mag-flow approach. Results show that the precision is significantly increased using the mag-flow approach (Fig 4).

4 Discussion

The originality of this study is to derive velocities and strain rates in the wall of a blood vessel with the mag-flow approach. The precision of the mag-flow approach is dramatically better than the one of the segmentation approach. This is especially emphasized for the derivation of strain rates (Fig. 4). The main reason for this poor behavior of the segmentation approach is the spatial resolution. In the *in vivo* experiment, the radius of the carotid artery is about 5 pixels (3 mm), which is not enough for a precise segmentation of the contours. A precision of 0.1 pixel can hardly be reached for $R(t)$ after interpolating the segmented contour by a circle. Thus, the strain may be evaluated with an precision of 0.1/5≈2%. Eventually, time differentiation over a time step of 1/41s leads to an uncertainty for the strain rate of nearly 1 s^{-1}, which is in agreement with the oscillations observed along the curve in Fig. 4b. Comparatively, precision for the mag-flow approach is estimated to about 0.01 s^{-1}.

It can also be noted that the precision of the segmentation approach is increased when the spatial resolution is improved. In the phantom experiment, the radius is about 20 pixels, *i.e.* 4 times the radius of the *in vivo* experiment. This is consistent with the fact that strain rates deduced from the segmentation approach have smaller oscillations in the phantom experiment (Fig. 4d) than in the *in vivo* experiment (Fig. 4b). Nevertheless, in both cases, the

mag-flow approach the more precise method.

The mag-flow approach can be compared to two other VVI approaches dedicated to vessel walls:

- [17] measured the velocity vectors in the wall of the thoracic aorta using PC-MRI and in-plane velocity encoding. This required the use of a special phased-array cardiac coil for reaching a pixel size of 0.39 mm. Moreover, spatial saturation was necessary in the axial direction for minimizing flow artifacts. Eventually, [17] were able to map the wall velocity with a remarkable precision. PC-MRI with in-plane velocity encoding is probably the most precise way for VVI in the artery wall. However, a limitation of this approach is the very stringent requirements regarding the pixel size (less than half of the artery thickness) and the minimization of flow artifacts.

- [10] measured the velocity vectors in the wall of the CCA in 43 human subjects using ultrasounds. Analysis consists first in tracking the border between the intima and the media throughout the whole cardiac cycle. Arterial wall is divided into 6 segments and the velocity vectors of each segment are derived from the variations over time of the position of the tracked intima-media border. The approach is simpler than a MRI-based approach but it is limited to the investigation of shallow arteries. Precision of this approach is not documented.

Apart from the two previously cited studies, VVI of artery walls remains scarce. This highlights the interest for simple and precise approaches that may be repeated on a large number of subjects. Indeed, knowledge of typical strain rate values in the arterial tissue is very important for characterizing and modeling the mechanical behavior of arteries. *In vitro* characterization of arteries is usually achieved in quasi-static conditions [24], whereas actual strain rates can reach nearly 0.7 s^{-1} (Fig. 4a). Moreover, [10] reported discrepancies between the strain rates of healthy and diseased CCA, which should be investigated further for different arteries.

5 Conclusion

In conclusion, a new approach has been presented for time-resolved measurements of wall velocity and strain rate in human arteries using MRI. The feasibility has been proved *in vitro* on an arterial phantom and *in vivo* on the CCA of a healthy subject.

Applications are now envisaged on other arteries, like the aorta, for example in aneurisms or after stenting. Regarding the carotid artery, the approach will be applied to patients having atherosclerotic plaques [12, 25] in order to assess the stability of the plaques thanks to the measurement of deformations and strain rates over a cardiac cycle.

Improvements of the approach are also under progress, possibly extending it to ultrasound techniques [7, 10]. Moreover, improvements of the MRI devices may also help to increase the spatial resolution of the technique for investigating small blood vessels.

6 Conflict of interest

None.

7 Acknowledgements

This study is part of the Imandef project (Grant ANR-08-JCJC-0071) funded by the ANR (French National Research Agency).

8 Appendix 1

8.1 The phantom experiment

Experiments on an arterial phantom made of silicone gel under pulsatile flow and pressure conditions were performed. The arterial phantom is a 50 cm silicon rubber tube. It has a 7-mm inner diameter and a 3.5-mm thickness. Pulsatile flow mimicking physiological pressure and flow was generated by a peristaltic pump while the wall motion was imaged. The arterial phantom was surrounded by a PVA gel (1 freeze-thaw-cycle), mimicking the surrounding tissue.

8.2 Obtaining magnitude images throughout the cardiac cycle

The MRI scanner used in our study is a 3T Siemens system (IRMAS, Saint-Etienne, France). A 2D spin-echo FLASH sequence [26] is used to acquire a single 3 mm thick slice with a matrix size of 256×256 giving in-plane dimensions 0.59×0.59 mm^2 for the *in vivo* experiment and 0.27×0.27 mm^2 for the phantom experiment. A cine sequence is used to acquire the temporal evolution of the flow throughout the pulse. Heart beats are detected by the measurement of blood flow in the subject's finger with near infrared spectrometry. The cine data are reconstructed to give N snapshots evenly distributed throughout the cardiac cycle. For the *in vivo* experiment, N=42, corresponding to a mean sampling frequency of 41 s^{-1} (T=1s). For the *in vitro* phantom experiment, N=50, corresponding to a mean sampling frequency of 49 s^{-1} (T=1s).

The magnitude of the signal is digitized with a 16 bits resolution (integer numbers between 0 and 65535).

Eventually, the magnitude image is a 3D array of size $256\times256\times N$, denoted $\widetilde{I}(x_p, y_q, t_n)$, for p varying from 1 to 256, q varying from 1 to 256 and n varying from 1 to N. A region of interest of 31×31 pixels is selected around

the vessel for the *in vivo* experiment. A region of interest of 61×61 pixels is selected around the vessel for the *in vitro* phantom experiment.

8.3 Origin of clinical data

All subjects sign an informed consent. Phase contrast MRI data and blood pressure are recorded successively following 15 min of recumbent rest in a room dedicated to echography. Data used herein are from two healthy subjects: a 23- year-old man (patient A) and a 26-year-old man (patient B).

For each patient, the imaging plane is a plane perpendicular to the axis of the CCA, located 24 mm below the carotid bifurcation. A cartesian reference frame is defined in this plane. The origin, denoted O, is at the centre of gravity of the artery at $t = t_1$. The $\vec{i}$ and $\vec{j}$ axis are respectively the horizontal and vertical axes in the imaging plane whereas the $\vec{k}$ axis is normal to the imaging plane. Let (x,y) denote the coordinates of a given point M in $(O,\vec{i},\vec{j})$.

In Fig. 1, the region of interest, which is located around the left hand side CCA, contains two zones of high intensity (bright zones) which correspond to zones containing blood. They are the internal jugular vein (largest zone) and the left CCA (with a nearly round shape).

8.4 Image processing

We have to deduce a continuous field $I(x,y,t)$ from the discrete data $\widetilde{I}(x_p,y_q,t_n)$.

First, the magnitude images are smoothed over time using a Gaussian filtering kernel in order to reduce the influence of noise. After filtering, one obtains:

$$\overline{I}(x_p,y_q,t) = \frac{\sum_{n=1}^{N} \widetilde{I}(x_p,y_q,t_n) W_t(t-t_n)}{\sum_{n=1}^{N} W_t(t-t_n)} \tag{7}$$

with:

$$W_t(t-t_n) = \exp(-(t-t_n)^2/R_t^2) + \exp(-[T-(t-t_n)]^2/R_t^2) + \exp(-[T+(t-t_n)]^2/R_t^2) \tag{8}$$

where T is the period of the signal and W_t is the Gaussian filtering kernel. It is actually the sum of three Gaussian filtering kernels in order to involve the preceding and following period of the signal in the following process. For instance, for filtering the data for $t = t_1$, the term $\exp(-(t-t_n)^2/R_t^2)$ give a significant weight to the data at $t > t_1$ whereas the term $\exp(-[T+(t-t_n)]^2/R_t^2)$ give a significant weight to the data at $t < t_1$, which are similar to the data for $t < t_N$. In this case, the term $\exp(-[T-(t-t_n)]^2/R_t^2)$ is negligible. Conversely, for filtering the data for $t = t_N$, the term $\exp(-(t-t_n)^2/R_t^2)$ give a significant weight to the data at $t < t_N$ whereas the term

$\exp(-[T-(t-t_n)]^2/R_t^2)$ give a significant weight to the data at $t > t_N$, which are similar to the data for $t > t_1$. In this case, the term $\exp(-[T+(t-t_n)]^2/R_t^2)$ is negligible.

Then, an interpolation method [27, 28] is used for reconstructing $I(x,y,t)$ for any x and y in the imaging plane, such as:

$$I(x,y,t) = \sum_p \sum_q W_x(x-x_p) W_y(y-y_p) \bar{I}(x_p,y_q,t) \tag{9}$$

where:

$$\begin{aligned} W_x(x-x_p) &= \frac{\exp(-(x-x_p)^2/R_x^2)}{256 \times N \times \sum_{p=1}^{256} \exp(-(x-x_p)^2/R_x^2)} \\ W_y(y-y_q) &= \frac{\exp(-(y-y_q)^2/R_y^2)}{256 \times N \times \sum_{q=1}^{256} \exp(-(y-y_q)^2/R_y^2)} \end{aligned} \tag{10}$$

R_x and R_y are chosen in order to control the filtering effect in each direction (trade-off between the search of a relevant filtering effect and the risk of spoiling local information). The choice for R_x and R_y is about the pixel size (the precise value of R_x and R_y may vary from one set of data to another) which means that the weighting functions act on the few pixels in the neighborhood of (x,y).

Eq. 9 gives a continuous and smooth representation of the intensity $I(x,y,t)$. From it, the partial derivatives $\frac{\partial I}{\partial x}(x,y,t)$, $\frac{\partial I}{\partial y}(x,y,t)$ and $\frac{\partial I}{\partial t}(x,y,t)$ can be deduced.

9 Appendix 2

9.1 The segmentation approach

Let us define the closed curve around O figuring all the points belonging to the vessel wall. The thickness of the vessel wall is neglected as it is approximately similar to the pixel size in the images. This justifies to represent the cross section of the vessel wall by a closed curve. This curve is denoted $\mathfrak{C}(t)$, where t denotes time. The curve changes its shape and size over time due to the varying blood pressure. The curve is defined in a polar way, such as $(x(t),y(t))$ belongs to this curve if:

$$\begin{cases} x(t) = r(\theta,t)\cos(\theta) \\ y(t) = r(\theta,t)\sin(\theta) \\ 0 \leq \theta \leq 2\pi \end{cases} \tag{11}$$

with a Fourier decomposition of $r(\theta,t)$ up to order N:

$$r(\theta,t) = \sum_{k=0}^{N} [a_k(t)\cos(k\theta) + b_k(t)\sin(k\theta)] \tag{12}$$

The values of $a_k(t)$ and $b_k(t)$ are determined at any time t like this:

1. the gradient of the magnitude is deduced like this:

$$\nabla\bar{I}(x_p,y_q,t)=\frac{1}{2}\sqrt{\left[\frac{\partial\bar{I}}{\partial x}(x_p,y_q,t)\right]^2+\left[\frac{\partial\bar{I}}{\partial y}(x_p,y_q,t)\right]^2} \tag{13}$$

The formula in Eq. 13 is not valid for the edges of the image but this does not concern the carotids which are sufficiently far from the edges so gradients on the edges are disregarded.

The obtained images of $\nabla\bar{I}$ show the largest gradients at the location of the artery wall.

2. Pixels belonging to the vessel wall are tracked as the pixels having the largest values in $\nabla\bar{I}(x_p,y_q,t)$. Indeed, due to the large quantity of blood flowing in the artery and also due to the distinct T_1 and T_2 relaxation parameters between blood and the surrounding tissues [16], the magnitude of the signal is larger inside the artery than outside. A segmentation algorithm based on the watershed approach [29] is developed for this using the Matlab software. Two source points are imposed: one at the corner of the image and one in the blood region (this point is imposed manually by a user through a graphical user interface). Let $(\tilde{x}_i(t),\tilde{y}_i(t))$ be the coordinates of the obtained points after segmentation.

3. Least squares regression is achieved. It consists in finding the coefficients $a_k(t)$ and $b_k(t)$ that minimize the following cost function:

$$J=\sum_i\left[\sum_{k=0}^{N}\left[a_k(t)\cos(k\tilde{\theta}_i(t))+b_k(t)\sin(k\tilde{\theta}_i(t))\right]-\tilde{r}_i(t)\right]^2 \tag{14}$$

where:

$$\begin{array}{l}\tilde{r}_i(t)=\sqrt{(\tilde{x}_i(t))^2+(\tilde{y}_i(t))^2}\\ \tilde{\theta}_i(t)=\arg((\tilde{x}_i(t))+j\,(\tilde{y}_i(t)))\\ j^2=-1\end{array} \tag{15}$$

Then, $r(\theta,t)$ defined in Eq. 12 is obtained and hence the curve defining the artery wall over time. The length of the curve is derived such as:

$$L(t)=\int_0^{2\pi}r(\theta,t)d\theta=2\pi a_0(t) \tag{16}$$

Eventually, the average strain of the artery at time t, considering the reference state at time t_1, is:

$$\varepsilon(t)=\frac{L(t)-L(t_1)}{L(t_1)}=\frac{a_0(t)-a_0(t_1)}{a_0(t_1)} \tag{17}$$

References

[1] J. Stalhand, A. Klarbring, and M. Karlsson. Towards in vivo aorta material identification and stress estimation. *Biomechanics and Modeling in Mechanobiology*, 2(3):169–186, 2004.

[2] C.A. Schulze-Bauer and G.A. Holzapfel. Determination of constitutive equations for human arteries from clinical data. *Journal of Biomechanics*, 36(2):165–169, 2003.

[3] R.W. Stadler, J.A. Taylor, and R.S. Lees. Comparison of B-mode, M-mode and echo-tracking methods for measurement of the arterial distension waveform. *Ultrasound in Medicine and Biology*, 23(6):879–887, 1997.

[4] V.R. Newey and D.K. Nassiri. Online artery diameter measurement in ultrasound images using artificial neural networks. *Ultrasound in Medicine and Biology*, 28(2):209–216, 2002.

[5] S.D. Kanters, O.E. Elgersma, J.D. Banga, M.S. Van Leeuwen, and A. Algra. Reproducibility of measurements of intima-media thickness and distensibility in the common carotid artery. *European Journal of Vascular and Endovascular Surgery*, 16(1):28–35, 1998.

[6] A.P. Hoeks, P.J. Brands, F.A. Smeets, and R.S. Reneman. Assessment of the distensibility of superficial arteries. *Ultrasound in Medicine and Biology*, 16(2):121–128, 1990.

[7] I. Masson, P. Boutouyrie, S. Laurent, J.D. Humphrey, and M. Zidi. Characterization of arterial wall mechanical behavior and stresses from human clinical data. *Journal of Biomechanics*, 41(12):2618–2627, 2008.

[8] K.V. Ramnarine, T. Hartshorne, Y. Sensier, M. Naylor, J. Walker, A.R. Naylor, R.B. Panerai, and D.H. Evans. Tissue doppler imaging of carotid plaque wall motion: a pilot study. *Cardiovascular Ultrasound*, 1:1–17, 2003.

[9] G. Valocik, L. Druzbacka, I. Valocikova, and P. Mitro. Velocity vector imaging to quantify left atrial function. *International Journal of Cardiovascular Imaging*, 26:641–649, 2010.

[10] In Jeong Cho, Young Shim Chi, Woo-In Yang, Sung-Ai Kim, Hyuk-Jae Chang, Yangsoo Jang, Namsik Chung, and Jong-Won Ha. Assessment of mechanical properties of common carotid artery in takayasu's arteritis using velocity vector imaging. *Circulation Journal*, 74:1465–1470, 2010.

[11] Zhanga Lei, Liub Yan, Zhanga Peng Fei, Zhaob Yu Xia, Ji Xiao Ping, Lub Xiao Ting, Chena Wen Qiang, Liua Chun Xi, Zhanga Cheng, and Zhanga Yun. Peak radial and circumferential strain measured by velocity vector

imaging is a novel index for detecting vulnerable plaques in a rabbit model of atherosclerosis. *Atherosclerosis*, 211:146–152, 2010.

[12] R.A. Baldewsing, C.L. De Korte, J.A. Schaar, F. Mastik, and A.F.W. Van Der Steen. Finite element modeling and intravascular ultrasound elastography of vulnerable plaques: parameter variation. *Ultrasonics*, 42:723–729, 2004.

[13] Z.-Y. Li, S. Howarth, R.A. Trivedi, J.M. U-King-Im, M.J. Graves, A. Brown, L. Wang, and J. Gillard. Stress analysis of carotid plaque rupture based on in vivo high resolution mri. *Journal of Biomechanics*, 39:2611–2622, 2006.

[14] E.A. Zerhouni, D.M. Parish, W.J. Rogers, A. Yang, and E.P. Shapiro. Human heart: tagging with MR imaging-a method for noninvasive assessment of myocardial motion. *Radiology*, 169:59–63, 1988.

[15] L. Axel and L. Dougherty. Mr imaging of motion with spatial modulation of magnetization. *Radiology*, 171:841–845, 1989.

[16] D.W. MacRobbie, E.A. Moore, M.J. Graves, and M.R. Prince. *MRI: From Picture to Proton*. Cambridge University Press, 2003.

[17] M.T. Draney, R.J. Herfkens, T.J.R. Hugues, N.J. Pelc, K.L. Wedding, C.K. Zarins, and C.A. Taylor. Quantification of vessel wall cyclic strain using cine phase contrast magnetic resonance imaging. *Annals of Biomedical Engineering*, 30:1033–1045, 2002.

[18] C.C. Moore, E.R. McVeigh, and E.A. Zerhouni. Quantitative tagged magnetic resonance imaging of the normal human left ventricle. *Topics in Magnetic Resonance Imaging*, 11:359–371, 2000.

[19] A.I. Veress, G.T. Gullberg, and J.A. Weiss. Measurement of strain in the left ventricle during diastole with cine-mri and deformable image registration. *ASME Journal of Biomechanical Engineering*, 127:1195–1207, 2005.

[20] N.F. Osman, E.R. McVeigh, and J.L. Prince. Imaging heart motion using harmonic phase mri. *IEEE Trans. Med. Imaging*, 19(3), 2000.

[21] S. Avril, J.M. Huntley, and R. Cusack. In-vivo measurements of blood viscosity and wall stiffness in the carotid using PC-MRI. *European Journal of Computational Mechanics*, 18(1):9–20, 2009.

[22] M.R. Moreno, J.E. Moore, and R. Meuli. Cross-sectional deformation of the aorta as measured with magnetic resonance imaging. *Journal of Biomechanical Engineering, Transactions of the ASME*, 120:18–21, 1998.

[23] S.S. Beauchemin and J.L. Barron. *The computation of optical flow*. ACM New York, 1995.

[24] A. Duprey, K. Khanafer, M. Schlicht, S. Avril, D. Williams, and R. Berguer. Ex vivo characterization of biomechanical behavior of ascending thoracic aortic aneurysm using uniaxial tensile testing. *European Journal of Vascular and Endovascular Surgery*, 39(6):700–707, 2010.

[25] S. Le Floc'h, J. Ohayon, P. Tracqui, G. Finet, A.M. Gharib, R.L. Maurice, G. Cloutier, and R.I. Pettigrew. Vulnerable atherosclerotic plaque elasticity reconstruction based on a segmentation-driven optimization procedure using strain measurements: theoretical framework. *IEEE Transactions on Medical Imaging*, 28(7):1126–1137, 2009.

[26] J.P. Hornak. *The basics of MRI*. http://www.cis.rit.edu/htbooks/mri, 2007.

[27] D. Shepard. A two-dimensional interpolation function for irregularly-spaced data. *Proceedings of the 1968 ACM National Conference*, pages 517–524, 1968.

[28] S. Avril, P. Feissel, F. Pierron, and Villon P. Comparison of two approaches for controlling the uncertainty in data differentiation: application to full-field measurements in solid mechanics. *Measurement Science and Technology*, 21(1):15703–15713, 2009.

[29] Matlab®. http://www.mathworks.com, 2008.

List of Figures

(a)

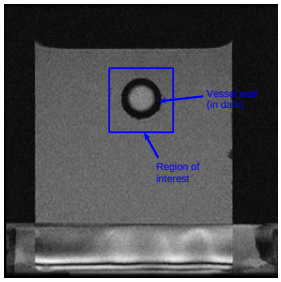

(b)

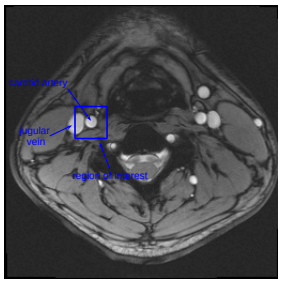

Figure 1: (a) Magnitude image of an arterial phantom (b) Magnitude image at the cross section of a subject's neck.

(a)

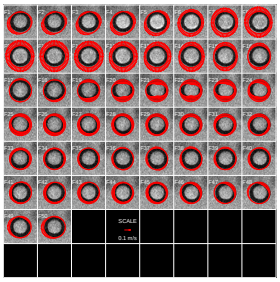

(b)

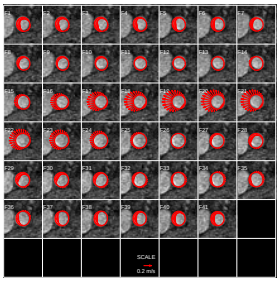

Figure 2: Contours of the artery and velocity vectors along this contour: (a) for the phantom experiment, (b) for the *in vivo* experiment. Sub-images labelled F*k*, with $k = 1$ to N, represent the magnitude image at the different times t_k throughout the cardiac cycle. The contours at each time t_k are deduced by the segmentation method. Arrows represent the local radial velocity, and the arrow length is scaled to the local velocity.

(a)

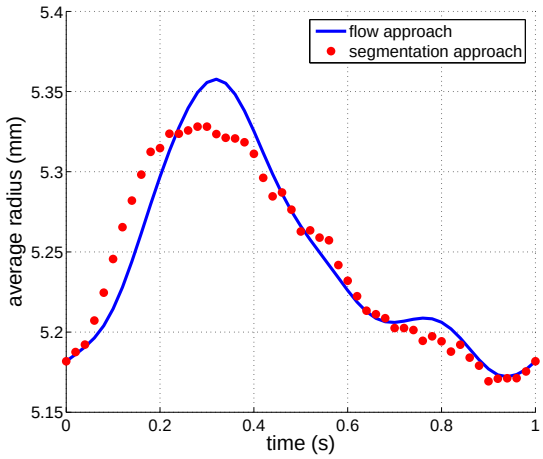

(b)

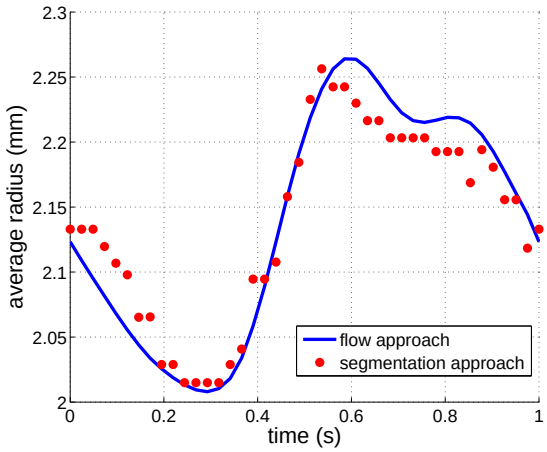

Figure 3: Comparison of the mag-flow approach and the segmentation approach for computing the average radius of the artery over time, (a) for the phantom experiment, (b) for the *in vivo* experiment.

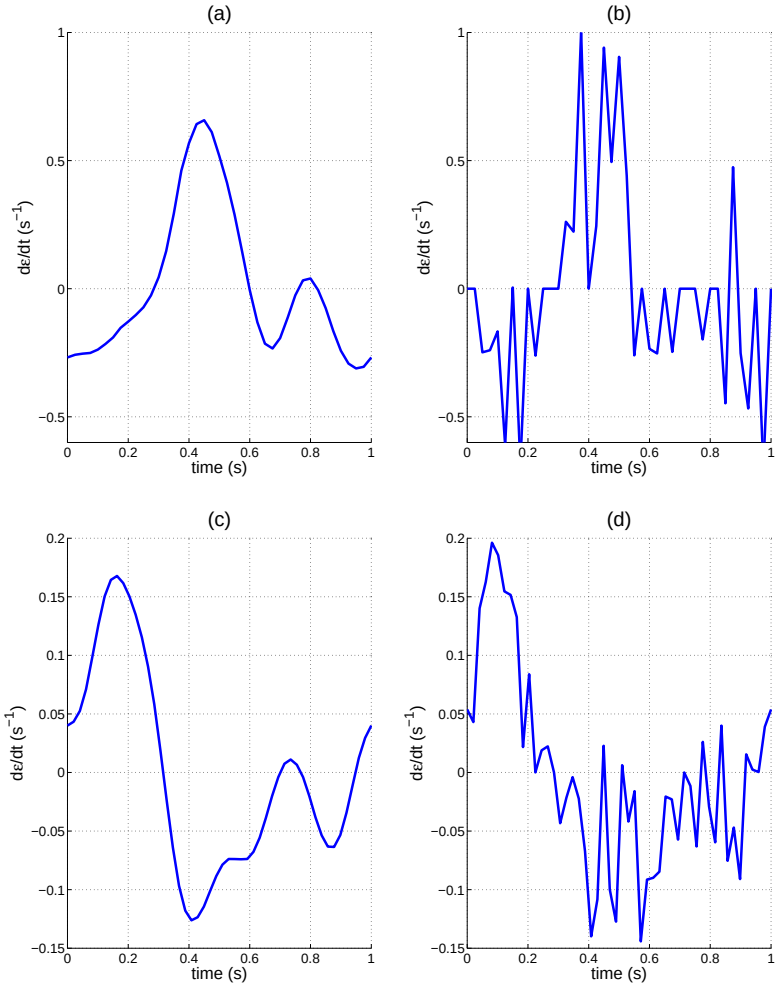

Figure 4: (a) Strain rate computed using the mag-flow approach in the *in vivo* experiment. (b) strain rate computed by the segmentation approach and time differentiation in the *in vivo* experiment. (c) Strain rate computed using the mag-flow approach in the phantom experiment. (d) strain rate computed by the segmentation approach and time differentiation in the phantom experiment.